Front. Phys.
https://doi.org/10.15302/frontphys.2027.053201
CN 11-5994/O4
ISSN 2095-0462

RESEARCH ARTICLE

Interference engineering for quantum imaginary-time evolution through multiple energy shifts

Hong-Jian Tang[1], Dan-Bo Zhang[1,2,*]

[1]Key Laboratory of Atomic and Subatomic Structure and Quantum Control (Ministry of Education), Guangdong Basic Research Center of Excellence for Structure and Fundamental Interactions of Matter, and School of Physics, South China Normal University, Guangzhou 510006, China

[2]Guangdong Provincial Key Laboratory of Quantum Engineering and Quantum Materials, Guangdong-Hong Kong Joint Laboratory of Quantum Matter, and Frontier Research Institute for Physics, South China Normal University, Guangzhou 510006, China

[*]Corresponding author. E-mail: dbzhang@m.scnu.edu.cn

Received August 23, 2026; accepted November 22, 2026

Energy shifting is usually trivial in imaginary-time evolution because it changes only the normalization of the evolved state. On a quantum computer, however, imaginary-time evolution can be implemented as a coherent or sampled superposition of real-time evolutions, in which energy shifts generate relative phases that can interfere. Here we introduce multi-shift quantum imaginary-time evolution (MS-QITE), which uses a distribution of energy shifts to engineer this interference and optimize different implementations. In a Monte Carlo realization, smooth Gamma and discrete energy shift distributions engineer finite-window interference, improving ground-state-energy estimation in selected regimes while balancing filtering and sampling fluctuations. In a continuous-variable-assisted realization, it enables projection onto finite-interval and Gamma modes, improving post-selection efficiency in identified accuracy regimes while retaining accurate thermal-state preparation. Numerical results for transverse-field Ising models and an XXZ spin chain demonstrate that energy shifts provide an interference-based degree of freedom for optimizing quantum imaginary-time evolution.

Keywords quantum algorithm, imaginary-time evolution, quantum interference

© Higher Education Press 2026

Just Accepted

This is a “Just Accepted” manuscript, which has been examined by the peer-review process and has been accepted for publication. A “Just Accepted” manuscript is published online shortly after its acceptance, which is prior to technical editing and formatting and author proofing. Higher Education Press (HEP) provides “Just Accepted” as an optional and free service which allows authors to make their results available to the research community as soon as possible after acceptance. After a manuscript has been technically edited and formatted, it will be removed from the “Just Accepted” Web site and published as an Online First article. Please note that technical editing may introduce minor changes to the manuscript text and/or graphics which may affect the content, and all legal disclaimers that

apply to the journal pertain. In no event shall HEP be held responsible for errors or consequences arising from the use of any information contained in these “Just Accepted” manuscripts. To cite this manuscript please use its Digital Object Identifier (DOI®), which is identical for all formats of publication.

Interference Engineering for Quantum Imaginary-Time Evolution through Multiple Energy Shifts

Hong-Jian Tang[1] and Dan-Bo Zhang[1, 2, *]

[1] *Key Laboratory of Atomic and Subatomic Structure and Quantum Control (Ministry of Education), Guangdong Basic Research Center of Excellence for Structure and Fundamental Interactions of Matter, and School of Physics, South China Normal University, Guangzhou 510006, China*

[2] *Guangdong Provincial Key Laboratory of Quantum Engineering and Quantum Materials, Guangdong-Hong Kong Joint Laboratory of Quantum Matter, and Frontier Research Institute for Physics, South China Normal University, Guangzhou 510006, China*

(Dated: October 20, 2026)

Energy shifting is usually trivial in imaginary-time evolution because it changes only the normalization of the evolved state. On a quantum computer, however, imaginary-time evolution can be implemented as a coherent or sampled superposition of real-time evolutions, in which energy shifts generate relative phases that can interfere. Here we introduce multi-shift quantum imaginary-time evolution (MS-QITE), which uses a distribution of energy shifts to engineer this interference and optimize different implementations. In a Monte Carlo realization, smooth Gamma and discrete energy-shift distributions engineer finite-window interference, improving ground-state-energy estimation in selected regimes while balancing filtering and sampling fluctuations. In a continuous-variable-assisted realization, it enables projection onto finite-interval and Gamma modes, improving postselection efficiency in identified accuracy regimes while retaining accurate thermal-state preparation. Numerical results for transverse-field Ising models and an XXZ spin chain demonstrate that energy shifts provide an interference-based degree of freedom for optimizing quantum imaginary-time evolution.

I. INTRODUCTION

Imaginary-time evolution (ITE) is a fundamental tool in quantum many-body physics and quantum chemistry [1–3]. By exponentially suppressing excited-state components, it provides a direct route to ground-state preparation, thermal-state preparation, and finite-temperature simulation [3–8]. In classical computation, ITE underlies or is closely connected to widely used approaches including quantum Monte Carlo and tensor-network methods [9–12].

For a Hamiltonian H and imaginary time τ, implementing ITE on a quantum computer is less direct because the operator $e^{-H\tau}$ is nonunitary and therefore cannot be realized as an ordinary gate-based evolution [2]. A broad range of strategies has therefore been developed. Variational formulations include variational QITE and related variational simulation principles [2, 13]. Local-unitary and circuit-based QITE approaches include the original QITE construction, practical QITE–Lanczos implementations, compressed-circuit evolution, double-bracket flows, Riemannian-gradient-flow constructions, and multi-copy unitary protocols [3, 14–18]. Deterministic or probabilistic realizations of the nonunitary map provide another route [19, 20], while Gibbs-state and finite-temperature preparation have been pursued through variational and sampling-based constructions [6–8, 21, 22]. Other approaches include linear-combination-of-unitaries methods [23–25] and Monte Carlo, algorithmic-cooling, and real-time-filtering methods [26–30]. Fourier-based cooling and generalized LCHS encompass broad families of real-time kernels [27, 31]. Thermal observables can also be reconstructed from sampled states and real-time dynamics [32], and ITE can be obtained by analytic continuation of real-time data [33]. Moreover, the imaginary-time evolution operator can also be constructed with an auxiliary continuous variable (CV) and postselection [34, 35].

Monte Carlo methods and continuous-variable-assisted methods provide two representative routes for implementing ITE through real-time quantum evolution. They estimate observables and prepare postselected states, respectively. However, both methods still suffer from practical limitations. In Monte Carlo approaches, the imaginary-time evolution is expressed as a weighted superposition of real-time evolutions, where the undamped Cauchy sampling distribution possesses a long-time tail. Consequently, long real-time evolutions can increase the Hamiltonian-simulation cost; phase cancellations also affect the variance of the normalized estimator. In continuous-variable-assisted methods, imaginary-time evolution is realized through the postselection of an auxiliary continuous-variable state. The choice of the projection state directly affects the success probability of the algorithm [34]. Designing more suitable projection states to improve the success probability without changing the imaginary-time evolution is therefore of practical interest.

A possible way to improve these algorithms comes from the idea of energy shifting. Energy shifts have been widely used in classical numerical algorithms, such as shift-and-invert methods for eigenvalue problems, where they modify spectral properties to improve computational performance [36, 37]. For conventional imaginary-time evolution, however, adding a constant energy shift only introduces an overall normalization factor and therefore

* dbzhang@m.scnu.edu.cn

does not change the final normalized state. On quantum computers, this invariance provides freedom in the real-time representation. Since many quantum implementations express imaginary-time evolution as a superposition of real-time evolutions [38], an energy shift appears as an additional phase factor in the real-time representation rather than merely an overall normalization. This observation provides additional freedom for algorithm design and opens up new possibilities for optimizing quantum implementations of imaginary-time evolution.

Motivated by this observation, we propose multi-shift quantum imaginary-time evolution (MS-QITE). Instead of applying a single constant energy shift, we introduce a distribution of energy shifts characterized by a function $f(q)$. Although the normalized imaginary-time evolution remains unchanged, the resulting complex interference kernel in the real-time representation can be tailored to optimize different quantum implementations. We demonstrate the application of the proposed approach to both Monte Carlo and continuous-variable-assisted imaginary-time evolution, as summarized in Fig. 1. For Monte Carlo methods, an appropriate multi-shift function reshapes the sampling distribution and shortens the effective real-time evolution, with smooth and discrete shift distributions offering different tradeoffs between finite-window filtering and sampling fluctuations. For continuous-variable-assisted methods, multi-shift is realized through the choice of the projection state, which admits an analytic success-probability optimum for a fixed ideal resource and half-axis projection class. Numerical simulations of ground-state-energy estimation and thermal-state preparation show how these benefits depend on the time window, sample budget, and tolerated state error. These results show that multi-shift provides a flexible algorithmic perspective for designing quantum imaginary-time evolution with explicit implementation-dependent tradeoffs.

The remainder of this paper is organized as follows. Sec. II introduces the multi-shift formulation. Sec. III presents Monte Carlo estimation, comparing Gamma and three-point shifts in Secs. III A and III B. Sec. IV presents the continuous-variable-assisted implementation and its application to thermal-state preparation. Sec. V concludes the paper.

II. MULTI-SHIFT FORMULATION

Let H be a Hermitian Hamiltonian with nonnegative spectrum, $\tau > 0$ the imaginary time, and $|\psi(0)\rangle$ a normalized initial state. If the physical Hamiltonian is not nonnegative, a constant multiple of the identity can first be added; this does not change the normalized imaginary-time-evolved state. Specifically, we use $H = H_{\text{phys}} - \ell I \succeq 0$, where ℓ is any known lower bound on the spectrum. The exact ground energy is not required: for a Pauli expansion $H_{\text{phys}} = \sum_\nu h_\nu P_\nu$, $\ell = -\sum_\nu |h_\nu|$ always suffices. Thus the requirement of a known spectral lower bound excludes no finite-dimensional Hermitian

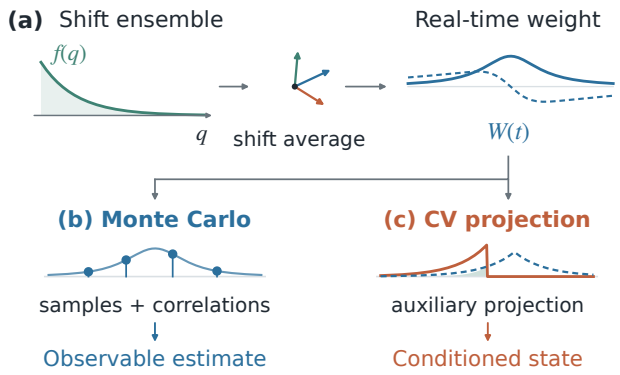


FIG. 1. The MS-QITE principle and its two implementations. (a) The shift distribution $f(q)$ determines the complex weight $W(t)$ through interference between shifted real-time evolutions. (b) Monte Carlo samples and quantum correlations give an observable estimate. (c) Projection of a CV auxiliary mode prepares a conditioned quantum state. In (a), solid/dashed blue curves show the real/imaginary parts of $W(t)$; in (c), the orange projection overlaps the dashed translated resource. The curves are illustrative.

Hamiltonian, although its tightness may affect implementation cost. The normalized evolution is

$$|\psi(\tau)\rangle = \frac{e^{-H\tau}|\psi(0)\rangle}{\sqrt{\langle\psi(0)|e^{-2H\tau}|\psi(0)\rangle}}. \tag{1}$$

For a single real energy shift b, replacing H by $H + bI$, where I is the identity operator, multiplies the unnormalized state by $e^{-b\tau}$ and therefore leaves Eq. (1) unchanged after normalization. More generally, let $f(q) \geq 0$ be a normalized distribution of energy shifts q on a support S, with $\int_S dq\, f(q) = 1$. Provided that $H + qI$ has nonnegative spectrum for every $q \in S$, one has

$$\int_S dq\, f(q) e^{-(H+qI)\tau} = C_f(\tau) e^{-H\tau},$$
$$C_f(\tau) \equiv \int_S dq\, f(q) e^{-q\tau} > 0. \tag{2}$$

Thus, the shift distribution changes only an overall scalar in imaginary time, while leaving the normalized state invariant. We assume $C_f(\tau) < \infty$. Negative shifts are allowed if the known spectral margin keeps $H + qI$ nonnegative throughout the support.

For a nonnegative Hamiltonian, the scalar identity $e^{-E\tau} = \int_{-\infty}^{\infty} dt\, g_\tau(t) e^{-iEt}$ for $E \geq 0$ extends spectrally to

$$e^{-H\tau} = \int_{-\infty}^{\infty} dt\, g_\tau(t) e^{-iHt}, \quad g_\tau(t) \equiv \frac{\tau}{\pi(\tau^2 + t^2)}. \tag{3}$$

Here $g_\tau(t)$ is the normalized Cauchy density. Applying Eq. (3) to each shifted Hamiltonian gives

$$\int_S dq\, f(q) e^{-(H+qI)\tau} = \int_{-\infty}^{\infty} dt\, g_\tau(t) W(t) e^{-iHt}, \tag{4}$$

where $W(t) \equiv \int_S dq\, f(q) e^{-iqt}$ is the characteristic function of the shift distribution. Equations (2) and (4) show the central point of MS-QITE: the same normalized imaginary-time evolution can be represented by different real-time interference kernels $g_\tau(t)W(t)$. The probability-distribution restriction is deliberate: in imaginary time, the shifted contributions have positive weights and are scalar multiples of the same operator, so they do not cancel. In the real-time representation, by contrast, the phases e^{-iqt} interfere. Signed or complex shift weights could enlarge the design space when $C_f(\tau) \neq 0$, but would introduce cancellations through the weights themselves; we leave them for future study.

Fourier-based quantum cooling already uses complex real-time weights [27], while Gaussian-damped Monte Carlo ITE and Gaussian filtering tailor spectral filters [26, 30]. Generalized LCHS provides broader exact representations of nonunitary dynamics and studies kernel decay and query complexity [25, 31]. Our positive-shift kernels form a structured subclass of that framework. However, the present construction starts from the invariance of normalized ITE under scalar energy shifts, using admissible positive shift ensembles as a physical design variable for both finite-window Monte Carlo estimation and CV projection. The ensuing objectives concern filtering bias, sampling fluctuations, and fixed-resource postselection rather than universal asymptotic complexity. The CV construction extends squeezed-postselection approaches [34], while related interference engineering also appears in coherent transport [39, 40].

A useful example for both implementations is the Gamma distribution,

$$
\begin{aligned}
f_\Gamma(q) &= \frac{a^k}{\Gamma(k)} q^{k-1} e^{-aq}, \quad q \geq 0, \\
W_\Gamma(t) &= \left(\frac{a}{a+it}\right)^k, \quad C_\Gamma(\tau) = \left(\frac{a}{a+\tau}\right)^k,
\end{aligned} \tag{5}
$$

with $a, k > 0$; k need not be an integer. Both transforms follow from the same Gamma integral, $\int_0^\infty dq\, q^{k-1} e^{-zq} = \Gamma(k)/z^k$ for $\mathrm{Re}\, z > 0$. The phase is $\theta(t) = -k \arctan(t/a)$, while $|W_\Gamma(t)| = [1 + (t/a)^2]^{-k/2}$ suppresses the long-time tail. The two parameters therefore control attenuation and phase together. After rescaling and normalization, the case $a = \tau$ with positive integer k reproduces the rational LCHS kernel of Ref. [31] (Appendix C, $p = k+1$). We set $\hbar = 1$; t, τ, a have inverse-energy units.

The two implementations use this freedom differently: $W(t)$ determines Monte Carlo sampling weights for observable estimation (Sec. III) and the auxiliary CV projection for conditional state preparation (Sec. IV), as illustrated in Fig. 1. Their ideal normalized target is common; finite real-time windows and CV resources introduce different errors.

III. MULTI-SHIFT MONTE CARLO IMPLEMENTATION

Using Monte Carlo sampling, expectation values after imaginary-time evolution can be evaluated through a quantum–classical hybrid approach. For a Hermitian observable O and an initial state $|\psi_0\rangle$, the real-time representation gives a ratio of averaged quantum correlations. With multi-shift, the modulus of $W(t)$ is absorbed into the sampling distribution. For a finite cutoff T, we use

$$
\begin{aligned}
p_{W,T}(t) &= \frac{g_\tau(t)|W(t)|}{Z_{W,T}}, \\
Z_{W,T} &= \int_{-T}^{T} dt\, g_\tau(t)|W(t)|,
\end{aligned} \tag{6}
$$

on $[-T, T]$, with zero density outside. A practical estimator is obtained as follows:

1. On a classical computer, draw N independent pairs (t_l, t_l') from the chosen sampling distribution.

2. On a quantum computer, prepare $|\psi_0\rangle$ and estimate $\mu_l(O) = \langle\psi_0| e^{iHt_l'} O e^{-iHt_l} |\psi_0\rangle$ and $\mu_l(I)$. For a Pauli observable these complex amplitudes can be obtained from Hadamard tests, measuring real and imaginary parts separately; a general observable is first decomposed into a linear combination of Pauli terms.

3. Combine the measured correlations with the sample-dependent phase $\Phi_l = e^{i[\theta(t_l) - \theta(t_l')]}$, where $W(t)/|W(t)| = e^{i\theta(t)}$, to form

$$
\widehat{O}_{W,T} = \mathrm{Re} \frac{\sum_{l=1}^N \Phi_l \mu_l(O)}{\sum_{l=1}^N \Phi_l \mu_l(I)}. \tag{7}
$$

The factors $Z_{W,T}^2$ cancel in the ratio. This protocol estimates an observable without preparing the imaginary-time-evolved state. Its finite-window target is the expectation in the state filtered by $A_{W,T} = \int_{-T}^{T} dt\, g_\tau(t) W(t) e^{-iHt}$, provided $A_{W,T}|\psi_0\rangle \neq 0$. At zeros of W, the sampling weight is zero and its phase is immaterial; Gamma has no finite-time zeros. The omitted tail produces a systematic cutoff error that vanishes as the cutoff increases. Sampling adds a separate error, and a small sample denominator can make the ratio unstable. A narrower time distribution therefore does not by itself imply lower variance. We compare with the unmodified Cauchy kernel, $W = 1$, using the same positivity shift in both methods; this isolates the effect of multi-shift, rather than benchmarking the full Gaussian-damped algorithm of Ref. [26].

A common application of imaginary-time evolution is ground-state-energy estimation. In our simulations we use the open-boundary transverse-field Ising Hamiltonian

$$
H_{\mathrm{phys}} = -J \sum_{i=1}^{n-1} X_i X_{i+1} - h \sum_{i=1}^{n} Z_i, \tag{8}
$$

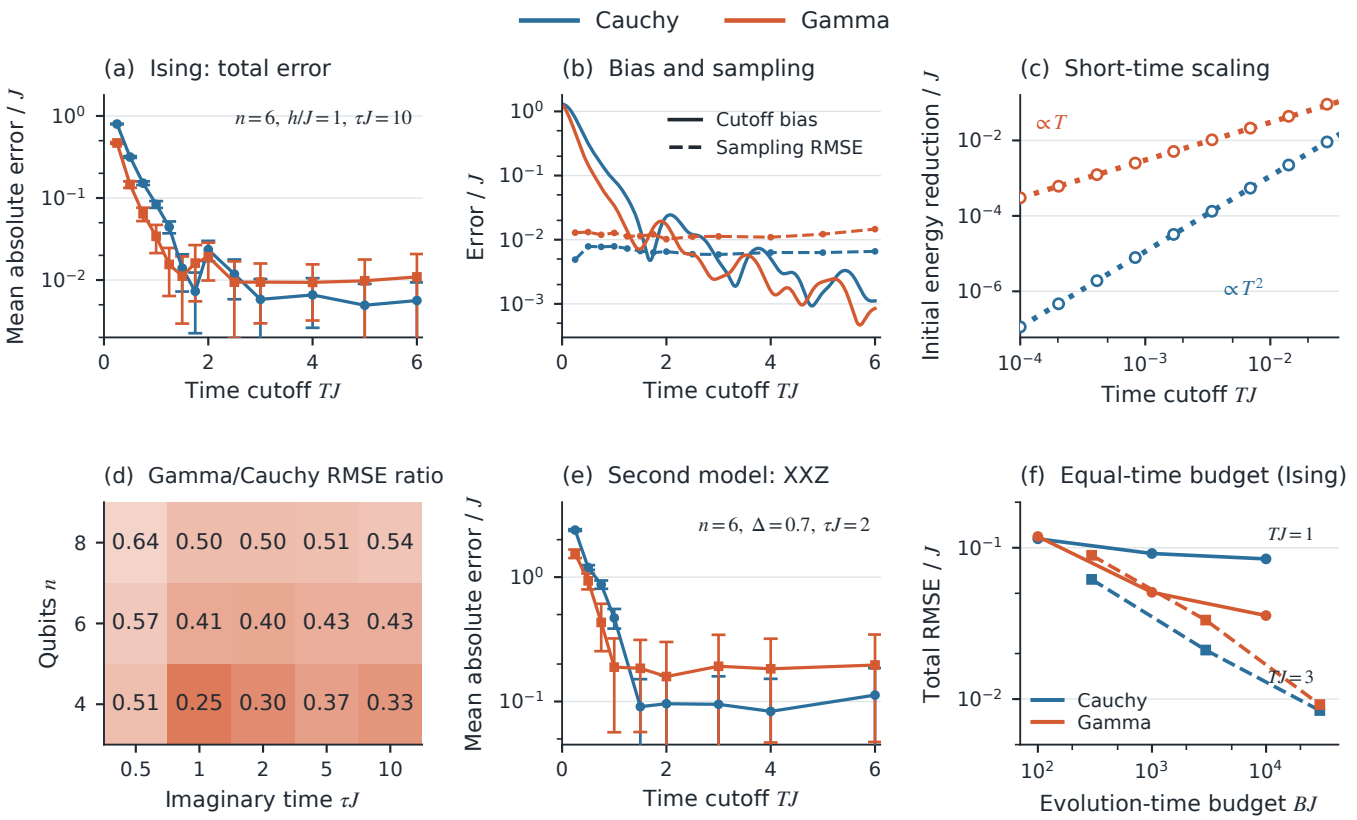


FIG. 2. Monte Carlo benchmarks with $k = 1/2$, $a = 0.1T$ and a shared positivity shift. Blue: Cauchy ($W = 1$); orange: Gamma. (a)–(c) Six-spin Ising chain, $h/J = 1$, $\tau J = 10$: mean absolute ground-energy error, cutoff bias (solid) versus sampling RMSE (dashed), and short-time energy reduction (open circles: numerically evaluated filter; dotted curves: leading-order asymptotes). (d) Gamma/Cauchy total-RMSE ratios across n and τ at $h/J = 1$, $TJ = 1$; values below one favor Gamma. (e) Six-spin XXZ chain, $\Delta = 0.7$, Néel input, $\tau J = 2$. Panels (a),(d),(e), and the sampling RMSE in (b), use 10^4 sampled time pairs and 80 independent repetitions. In (a),(e), error bars denote one standard deviation of the individual absolute errors across repetitions (not the standard error of the displayed mean). (f) The same Ising chain at equal expected evolution-time budget $B = N\mathbb{E}(|t| + |t'|)$; circles/solid lines: $TJ = 1$, squares/dashes: $TJ = 3$. Ising inputs are $|0\rangle^{\otimes n}$. Correlations use exact real-time evolution; measurement noise is excluded.

where n is the number of spins, J is the nearest-neighbor Ising coupling, h is the transverse field, and X_i, Y_i, Z_i are Pauli operators on site i. The initial state is $|0\rangle^{\otimes n}$, and the energy observable remains the unshifted H_{phys}. The bound ℓ in $H = H_{\text{phys}} - \ell I \succeq 0$ comes from a checked local semidefinite relaxation with overlapping three-site blocks [41]; the exact ground energy is used only as a reference. We test $n = 4, 6, 8$ and several fields and imaginary times. Each finite-sample point uses 10^4 sampled time pairs and 80 independent repetitions unless stated otherwise. Correlations are evaluated exactly, so Fig. 2 contains no quantum shot noise or device noise.

The real-time evolutions can be implemented using standard product formulas [42]. Writing Eq. (8) as $H_X + H_Z$, a first-order approximation for $t \geq 0$ is

$$U_r(t) = e^{i\ell t}\left(e^{-iH_X t/r} e^{-iH_Z t/r}\right)^r, \tag{9}$$

with $U_r(-t) = U_r(t)^\dagger$. An uncontrolled evolution uses $2(n-1)r$ CNOTs; Hadamard-test control adds overhead. Distributions favoring shorter sampled times can reduce average evolution cost, while the largest allowed duration remains T for every distribution. Direct product-formula checks for the Cauchy and Gamma kernels converge with increasing r; both have additional energy bias below $3 \times 10^{-3} J$ at $TJ = 3, r = 64$. These checks support finite-gate implementation, with the useful resource saving depending on the required final accuracy and sampling budget.

A. Gamma-distributed shifts

We first use the smooth Gamma shift distribution of Eq. (5). Its phase is $\theta(t) = -k \arctan(t/a)$, and its untruncated sampling density has the long-time tail $p_W(t) \sim |t|^{-k-2}$. Set $a = \rho T$ with $\rho > 0$. For $0 < k < 1$, symmetry gives the mean-phase bound

$$m_\theta \equiv \mathbb{E}_{p_{W,T}} \cos\theta(t) \geq \cos[k \arctan(1/\rho)] > 0. \tag{10}$$

We take $k = 1/2$ to balance tail suppression and phase cancellation. Let $E_{\rm init}$ and $V_{\rm init}$ be the initial physical energy and its variance. At fixed ρ, τ, with $T/\tau \ll 1$ and $T\|H\| \ll 1$,

$$E_{\Gamma,T} = E_{\rm init} - 2\eta(\rho)TV_{\rm init} + O(T^2),$$
$$\eta(\rho) = \frac{\sqrt{1+\rho^2}-\rho}{3}. \tag{11}$$

Here $E_{W,T}$ is the deterministic filtered energy; the Cauchy baseline has $E_{1,T} = E_{\rm init} + O(T^2)$. The choice $\rho = 0.1$ gives $\eta \simeq 0.302$, about 90% of its limiting value 1/3, and $m_\theta \geq 0.741$. This quantitative prescription $k = 1/2$, $a = 0.1T$ is fixed throughout; scans assess sensitivity rather than fit individual models. The phase bound does not control quantum overlaps in the full estimator or guarantee minimum variance.

For $n = 6$, $h/J = 1$, and $\tau J = 10$, the initial energy is $E_{\rm init} = -6J$. The cutoff bias in Fig. 2(b) is $|E_{W,T} - E_\tau|$, where E_τ is the exact ITE energy. Figure 2(c) verifies the linear and quadratic short-time behavior predicted above. The shift-induced interference thus allows energy lowering at first order in the available real time.

This stronger filtering competes with sampling fluctuations. At $TJ = 1$, Gamma lowers the mean absolute ground-energy error from $0.084J$ to $0.034J$, while sampling RMSE increases from $7.9 \times 10^{-3}J$ to $1.3 \times 10^{-2}J$ [Fig. 2(a),(b)]. At $TJ = 3$, the total RMSE ordering reverses. Across the tested grid, Gamma improves short-window bias in many cases but has larger empirical signed-estimator variance in every paired comparison. Panel (d) shows the Gamma/Cauchy total-RMSE ratio across sizes and imaginary times; values below one favor Gamma. Small relevant gaps and weak initial ground-state overlap still require larger imaginary time; these small-system results do not establish favorable asymptotic scaling.

The open XXZ chain, $H_{\rm phys} = J\sum_i (X_iX_{i+1} + Y_iY_{i+1} + \Delta Z_iZ_{i+1})$, gives the same qualitative tradeoff [Fig. 2(e)]. With $n = 6$, $\Delta = 0.7$, Néel input, and $\tau J = 2$, Gamma lowers the mean absolute error at $TJ = 1$, while the ordering reverses at $TJ = 3$. Increasing the sample number reduces statistical error toward the deterministic floor. Panel (f) compares Cauchy (blue) with Gamma (orange) for the same six-spin Ising chain at equal expected evolution time, $B = N\mathbb{E}(|t| + |t'|)$. Gamma uses about 1.25 times more pairs because its mean sampled time is shorter. Measurement and control overheads are excluded.

B. Three-point interference engineering

The shift distribution need not be continuous. As a complementary example to Gamma filtering, consider three nonnegative shifts selected for the real-time window $[-T, T]$, with $0 < \lambda \leq 1/2$:

$$f_{\lambda,T}(q) = (1-\lambda)\delta(q) + \frac{\lambda}{2}\sum_{\nu=1,3}\delta\Big(q - \frac{\nu\pi}{T}\Big). \tag{12}$$

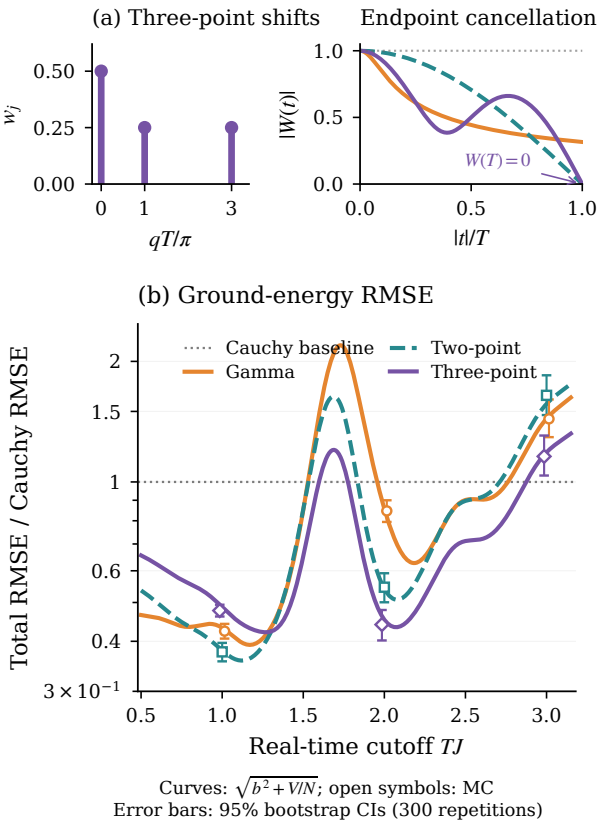


FIG. 3. Discrete-shift interference engineering. (a) A three-point positive shift distribution with $\lambda = 1/2$ and its characteristic-function modulus; the endpoint vanishes. Two-point endpoint cancellation and Gamma are shown for comparison. (b) Total ground-energy RMSE relative to unshifted Cauchy sampling in the six-spin Ising chain ($J = h = 1$, $\tau J = 10$, $N = 10^4$ sampled time pairs). All kernels use the same spectral lower bound. Curves use the large-sample $\sqrt{b^2 + V/N}$ prediction with full numerator–denominator covariance; open symbols give 300 independent Monte Carlo estimates, with 95% bootstrap confidence intervals. Quantum measurement-shot, Trotter, and hardware errors are excluded.

The corresponding weight is $W_{\lambda,T}(t) = 1 - \lambda + (\lambda/2)(e^{-i\pi t/T} + e^{-3i\pi t/T})$. Its shifts preserve the ideal normalized ITE map. The weight W is computed classically before time sampling, so the three components need not be implemented as three independent quantum evolutions.

At $\lambda = 1/2$, interference gives $W_{\lambda,T}(\pm T) = 0$ [Fig. 3(a)]. For fixed T, integration by parts then suppresses the generic high-energy boundary contribution of the truncated scalar filter from $O(E^{-1})$ to $O(E^{-2})$. This is distinct from the short-time expansion. Since the nonzero shifts scale as $1/T$, their phases remain finite when $t = Tu$.

For $T/\tau \ll 1$ and $T\|H\| \ll 1$, one obtains

$$E_{\lambda,T} = E_{\text{init}} - 2\eta_\lambda T V_{\text{init}} + O(T^2),$$
$$\eta_\lambda = \frac{2\lambda}{3\pi(1-\lambda)}. \tag{13}$$

Here V_{init} is the initial energy variance. At $\lambda = 1/2$, $\eta_\lambda \simeq 0.212$; the corresponding Gamma value is 0.302. Thus the cancellation improves large-energy filtering while the leading short-window cooling term is still linear in T, rather than quadratic.

Figure 3(b) compares the total ground-energy RMSE at a common cutoff and 10^4 sampled time pairs. At $TJ = 2$, the three-point kernel gives approximately $0.011J$, compared with $0.020J$ for Gamma and $0.024J$ for unshifted Cauchy sampling; direct Monte Carlo results agree. A two-point kernel with equal weights at $q = 0, \pi/T$ also cancels the endpoints but gives a larger total RMSE (about $0.013J$). The three-point rule has slightly more filtering bias yet smaller sampling fluctuations than that two-point control. Relative performance changes with the cutoff, so endpoint cancellation alone does not guarantee a global optimum. These atomic distributions illustrate the Monte Carlo branch; they do not directly define normalizable CV projection wavefunctions.

IV. CONTINUOUS-VARIABLE-ASSISTED MULTI-SHIFT IMPLEMENTATION

We next consider a fully quantum implementation assisted by one continuous-variable (CV) mode. Let $\hat{x}$ and $\hat{p}$ be canonically conjugate quadratures with $[\hat{x}, \hat{p}] = i$, and use the Fourier convention $\langle x|p\rangle = (2\pi)^{-1/2} e^{ipx}$. Quadratures are scaled so that $H\hat{p}$ and $\tau\hat{x}$ are dimensionless. The system Hamiltonian H is again taken to have nonnegative spectrum, after a constant shift if necessary. Define the normalized resource state

$$|R_\tau\rangle = \sqrt{2\pi\tau} \int dp\, g_\tau(p)|p\rangle,$$
$$R_\tau(x) = \sqrt{\tau} e^{-\tau|x|}. \tag{14}$$

The protocol is:

1. Prepare the system state (or a purification of a mixed state) and the CV resource state $|R_\tau\rangle$.
2. Apply the joint unitary $e^{-iH\hat{p}}$.
3. Project the CV mode onto a normalized state $|\phi\rangle$.

Conditioned on successful projection, the system is acted on by the Kraus operator

$$K_\phi = \sqrt{2\pi\tau} \int dp\, g_\tau(p)\phi^*(p) e^{-iHp}. \tag{15}$$

Hence, if $\phi^*(p)$ is proportional to a desired $W(p)$, the postselected state realizes the corresponding MS-QITE kernel. The proportionality constant affects the success probability but not the normalized output.

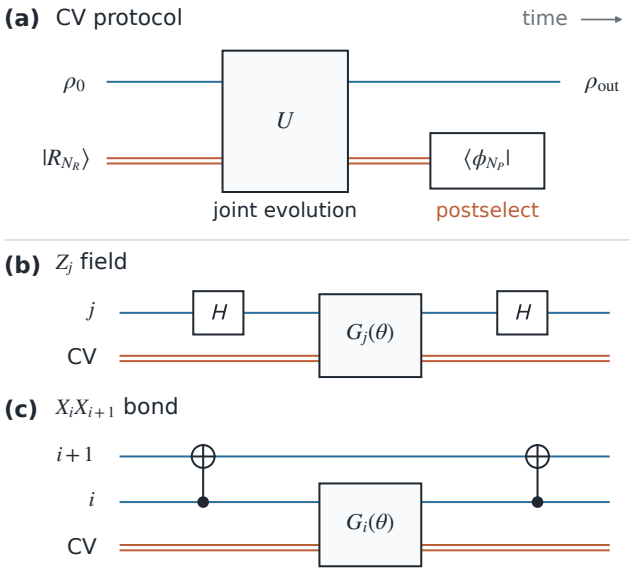


FIG. 4. CV protocol and elementary gates. (a) Joint evolution $U = e^{-i(H_{\text{phys}} - \ell I)\hat{p}}$ followed by projection prepares ρ_{out}. (b),(c) Hadamard and CNOT conjugations of $G_j(\theta) = e^{-i\theta X_j \hat{p}}$ give the Ising field and bond factors [34], with $\theta = -h/r$ and $-J/r$ for r steps. The local identities are exact; their product approximates the joint evolution. Single blue lines denote qubits and double orange lines the CV mode.

In our previous work, a squeezed projection state was used for thermal-state preparation [34]. Finite squeezing creates a tradeoff between thermal-state accuracy and postselection probability. The multi-shift viewpoint shows that one need not restrict the projection to a narrow Gaussian. A particularly simple choice is the normalized step-function state, with wavefunction $\phi_L(x) = 1/\sqrt{L}$ on $[-L, 0]$ and zero elsewhere. It corresponds to the uniform positive-shift distribution on $[0, L]$ and gives

$$K_L = \frac{1 - e^{-L\tau}}{\sqrt{L\tau}} e^{-\tau H},$$
$$P_L = \frac{(1 - e^{-L\tau})^2}{L\tau} Q_\tau, \tag{16}$$

where $Q_\tau = \text{tr}(\rho_0 e^{-2\tau H})$ for input ρ_0. Thus L changes only the postselection amplitude. The optimal width satisfies $L\tau \simeq 1.256$, giving $P_L^{\max} \simeq 0.407 Q_\tau$.

The Gamma family extends this construction. More generally, a square-integrable shift density on $q \geq 0$ defines the normalized half-axis projection $\phi_f(x) = f(-x)/\|f\|_2$ for $x \leq 0$, and gives

$$P_f = \frac{\tau C_f(\tau)^2}{\|f\|_2^2} Q_\tau. \tag{17}$$

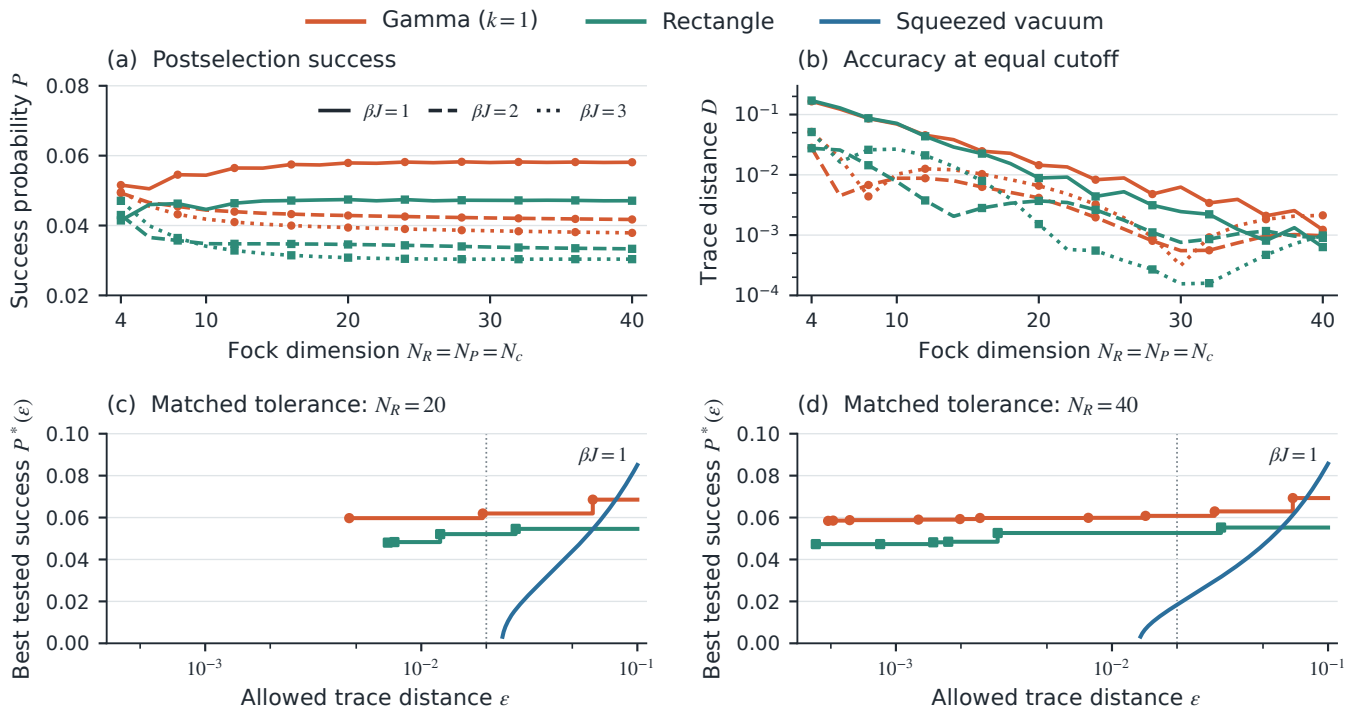


FIG. 5. Thermal-state preparation for the four-spin Ising chain with $J = h = 1$, $\rho_0 = I/16$, $\beta = 2\tau$, and $\ell \simeq -4.775J$. Gamma uses $k = 1, a = \tau$; rectangles use $L\tau = 1.256$. (a),(b) Success probability and trace distance at the common cutoff $N_R = N_P = N_c$. (c),(d) Largest tested success at a common trace-distance tolerance ϵ, with $\beta J = 1$ and fixed $N_R = 20, 40$. Rectangle/Gamma curves scan every $N_P = 2, \ldots, 40$; the origin-centered squeezed vacuum scans $s \in [1, 60]$ without a projection cutoff. Blank regions have no feasible tested parameter; dotted lines mark $\epsilon = 0.02$. Truncated states are normalized separately and joint evolution acts in the full CV space.

For Gamma, normalization requires $k > 1/2$, excluding the MC choice $k = 1/2$. Equation (17) gives

$$P_{k,a} = \frac{\tau(2a)^{2k-1}\Gamma(k)^2}{\Gamma(2k-1)(a+\tau)^{2k}} Q_\tau. \tag{18}$$

At fixed k, this is maximized by $a_\star = (2k-1)\tau$. For normalized projections on $x \le 0$, the factorization $R_\tau(x - E) = \sqrt{\tau} e^{\tau x} e^{-\tau E}$ and Cauchy–Schwarz give $P \le Q_\tau/2$. Equality is attained by $\phi(x) = \sqrt{2\tau} e^{\tau x}$, namely $k = 1$, $a = \tau$, improving ideal success by 22.8% over the best rectangle. Both parameters therefore follow analytically for the fixed ideal resource, rather than from a spectral scan; the finite-Fock tests retain this choice.

For thermal-state preparation, starting from the maximally mixed state $\rho_0 = I/2^n$ produces the Gibbs state $\rho_\beta = e^{-\beta H_{\rm phys}}/Z_\beta$ at $\tau = \beta/2$, where $Z_\beta = \operatorname{tr} e^{-\beta H_{\rm phys}}$. The constant positivity shift cancels from the normalized output but not from the postselection probability: here $Q_{\beta/2} = e^{\beta\ell} Z_\beta/2^n$. At low temperature, a small initial ground-state weight and a loose lower bound can strongly suppress success. A ground manifold of dimension d_0 has only weight $d_0/2^n$ in the maximally mixed input, leaving an exponential size cost when $d_0 = O(1)$. Multi-shift improves the projection prefactor while retaining this physical postselection cost.

For numerical implementation, both the projection and resource states are truncated in the Fock basis and renormalized. We use

$$|\chi_N\rangle = \mathcal{N}_N \sum_{m=0}^{N-1} c_m |m\rangle, \quad c_m = \langle m|\chi\rangle, \tag{19}$$

where $\mathcal{N}_N$ normalizes the state. The resource dimension N_R and projection dimension N_P count retained Fock levels $0, \ldots, N-1$. When equal, their common cutoff is $N_R = N_P = N_c$. The coefficients follow by integration against normalized Hermite functions; the even resource has only even Fock components. Ideal rectangular and exponential projection modes have divergent mean photon number. Their finite approximations make the resource cost explicit and introduce output error. Classical propagation does not restrict oscillator occupation to these preparation and projection cutoffs.

With a finite Fock cutoff, these states can be synthesized in a cavity as finite superpositions using qubit–cavity couplings, or number-dependent phases and displacement operations [43–46]. Figure 4 summarizes the protocol and elementary gates. Reversible synthesis prepares the resource; inverse synthesis of the projection mode followed by vacuum selection performs the projection. For the

Ising Hamiltonian, the elementary gate $G_j(\theta) = e^{-i\theta X_j \hat{p}}$ implements each field or bond factor using Hadamard or CNOT conjugation. Each first-order product-formula step uses $2n-1$ hybrid gates and $2(n-1)$ CNOTs, with the shift implemented as an unconditional displacement.

We next study thermal-state preparation for a four-qubit transverse-field Ising model, with $J = h = 1$ and the shared checked lower bound $\ell \simeq -4.775J$. We quantify the state error by the trace distance $D_{\mathrm{tr}}(\rho, \sigma) = \frac{1}{2}\|\rho - \sigma\|_1$. Figure 5(a),(b) compares the rectangle and $k = 1, a = \tau$ Gamma projection for several temperatures and equal Fock dimensions. At $\beta J = 1$, $N_R = N_P = 40$, their success probabilities are 0.047 and 0.058, while their trace distances are 6.3×10^{-4} and 1.2×10^{-3}. Gamma improves success here but has larger state error.

Panels (c),(d) therefore compare the largest tested success at a common error tolerance, scanning $N_P = 2, \ldots, 40$ for the two shapes while keeping their analytically chosen shape parameters fixed. The origin-centered squeezed vacuum instead scans its squeezing parameter $s \in [1, 60]$. Here $\phi_s(p) \propto e^{-p^2/(2s^2)}$, so larger s means stronger position squeezing. At $N_R = 40$ and tolerance 0.02, the rectangular, Gamma, and squeezed projections reach success probabilities 0.053, 0.061, and 0.018. At tolerance 0.1, squeezing instead reaches 0.086, exceeding Gamma's 0.069. The advantage thus depends on the required accuracy and the tested projection family. These curves use exact joint evolution. Finite-gate checks at $\beta J = 1$, $N_R = N_P = 40$ reduce the final Gibbs-state trace distance from about 8×10^{-3} to 2×10^{-3} for both modes as the number of product-formula steps increases from 32 to 128. The reported probabilities and errors exclude synthesis and control imperfections, oscillator loss, and readout inefficiency; these additional costs must be included in a hardware comparison.

V. CONCLUSION

We have introduced multi-shift quantum imaginary-time evolution (MS-QITE) as an optimization framework for quantum implementations of imaginary-time evolution. The key observation is that a distribution of energy shifts changes only an overall scalar in imaginary time but modifies the interference kernel in a real-time representation. In the Monte Carlo realization, Gamma shifts suppress long-time samples, whereas discrete shifts can cancel finite-window boundary contributions. Both improve filtering in identified regimes while retaining sampling-error trade-offs. In the continuous-variable-assisted realization, it maps directly to the choice of projection wavefunction and allows the success probability to be optimized over half-axis projections for a fixed ideal resource. Finite-Fock comparisons show that the advantage over centered squeezed projections depends on the tolerated state error. Numerical simulations for transverse-field Ising models, with an XXZ extension for Monte Carlo estimation, illustrate both mechanisms. The framework suggests several natural extensions, including optimization of shift distributions under hardware-specific cost functions, systematic accounting of state-preparation overhead, and scaling tests in larger systems.

ACKNOWLEDGMENTS

This work was supported by the National Natural Science Foundation of China (Grant Nos. 12375013 and 12547109) and by the Guangdong Provincial Quantum Science Strategic Initiative (Grant No. GDZX2503008).

[1] L. Lehtovaara, J. Toivanen, and J. Eloranta, Solution of time-independent Schrödinger equation by the imaginary time propagation method, J. Comput. Phys. **221**, 148 (2007).

[2] S. McArdle, T. Jones, S. Endo, Y. Li, S. C. Benjamin, and X. Yuan, Variational ansatz-based quantum simulation of imaginary time evolution, npj Quantum Inf. **5**, 75 (2019).

[3] M. Motta, C. Sun, A. T. K. Tan, M. J. O'Rourke, E. Ye, A. J. Minnich, F. G. S. L. Brandão, and G. K.-L. Chan, Determining eigenstates and thermal states on a quantum computer using quantum imaginary time evolution, Nat. Phys. **16**, 205 (2020).

[4] D. Poulin and P. Wocjan, Preparing ground states of quantum many-body systems on a quantum computer, Phys. Rev. Lett. **102**, 130503 (2009).

[5] S.-N. Sun, M. Motta, R. N. Tazhigulov, A. T. K. Tan, G. K.-L. Chan, and A. J. Minnich, Quantum computation of finite-temperature static and dynamical properties of spin systems using quantum imaginary time evolution, PRX Quantum **2**, 010317 (2021).

[6] K. Temme, T. J. Osborne, K. G. H. Vollbrecht, D. Poulin, and F. Verstraete, Quantum Metropolis sampling, Nature **471**, 87 (2011).

[7] D. Poulin and P. Wocjan, Sampling from the thermal quantum Gibbs state and evaluating partition functions with a quantum computer, Phys. Rev. Lett. **103**, 220502 (2009).

[8] J. Wu and T. H. Hsieh, Variational thermal quantum simulation via thermofield double states, Phys. Rev. Lett. **123**, 220502 (2019).

[9] S. Sorella, Generalized Lanczos algorithm for variational quantum Monte Carlo, Phys. Rev. B **64**, 024512 (2001).

[10] W. A. Lester, Jr. and B. L. Hammond, Quantum Monte Carlo for the electronic structure of atoms and molecules, Annu. Rev. Phys. Chem. **41**, 283 (1990).

[11] S. Baroni and S. Moroni, Reptation quantum Monte Carlo: A method for unbiased ground-state averages and imaginary-time correlations, Phys. Rev. Lett. **82**, 4745 (1999).

[12] F. Verstraete, V. Murg, and J. I. Cirac, Matrix product states, projected entangled pair states, and variational renormalization group methods for quantum spin systems,

Adv. Phys. **57**, 143 (2008).
[13] X. Yuan, S. Endo, Q. Zhao, Y. Li, and S. C. Benjamin, Theory of variational quantum simulation, Quantum **3**, 191 (2019).
[14] K. Yeter-Aydeniz, R. C. Pooser, and G. Siopsis, Practical quantum computation of chemical and nuclear energy levels using quantum imaginary time evolution and Lanczos algorithms, npj Quantum Inf. **6**, 63 (2020).
[15] S.-H. Lin, R. Dilip, A. G. Green, A. Smith, and F. Pollmann, Real- and imaginary-time evolution with compressed quantum circuits, PRX Quantum **2**, 010342 (2021).
[16] M. Gluza, J. Son, B. H. Tiang, R. Zander, R. Seidel, Y. Suzuki, Z. Holmes, and N. H. Y. Ng, Double-bracket quantum algorithms for quantum imaginary-time evolution, Phys. Rev. Lett. **136**, 020601 (2026).
[17] N. A. McMahon, M. Pervez, and C. Arenz, Equating quantum imaginary time evolution, Riemannian gradient flows, and stochastic implementations, Phys. Rev. Research **8**, 023024 (2026).
[18] T. Schwartzman, T. V. Zache, H. Pichler, and H. R. Sadeghpour, Imaginary time evolution and ground state preparation using unitary multi-copy protocols, PRX Quantum **7**, 033033 (2026).
[19] Y. Mao, M. Chaudhary, M. Kondappan, J. Shi, E. O. Ilo-Okeke, V. Ivannikov, and T. Byrnes, Measurement-based deterministic imaginary time evolution, Phys. Rev. Lett. **131**, 110602 (2023).
[20] T. Liu, J.-G. Liu, and H. Fan, Probabilistic nonunitary gate in imaginary time evolution, Quantum Inf. Process. **20**, 204 (2021).
[21] Y. Wang, G. Li, and X. Wang, Variational quantum Gibbs state preparation with a truncated Taylor series, Phys. Rev. Applied **16**, 054035 (2021).
[22] R. Sagastizabal, S. P. Premaratne, B. A. Klaver, M. A. Rol, V. Negîrneac, M. S. Moreira, X. Zou, S. Johri, N. Muthusubramanian, M. Beekman, C. Zachariadis, V. P. Ostroukh, N. Haider, A. Bruno, A. Y. Matsuura, and L. DiCarlo, Variational preparation of finite-temperature states on a quantum computer, npj Quantum Inf. **7**, 130 (2021).
[23] A. M. Childs and N. Wiebe, Hamiltonian simulation using linear combinations of unitary operations, Quantum Inf. Comput. **12**, 901 (2012).
[24] A. N. Chowdhury and R. D. Somma, Quantum algorithms for Gibbs sampling and hitting-time estimation, Quantum Inf. Comput. **17**, 41 (2017).
[25] D. An, J.-P. Liu, and L. Lin, Linear combination of Hamiltonian simulation for nonunitary dynamics with optimal state preparation cost, Phys. Rev. Lett. **131**, 150603 (2023).
[26] M. Huo and Y. Li, Error-resilient Monte Carlo quantum simulation of imaginary time, Quantum **7**, 916 (2023).
[27] P. Zeng, J. Sun, and X. Yuan, Universal quantum algorithmic cooling on a quantum computer (2021), arXiv:2109.15304 [quant-ph].
[28] Y. Yang, Y. Li, X. Xu, and X. Yuan, Resource-efficient quantum-classical hybrid algorithm for energy gap evaluation, Phys. Rev. A **109**, 052416 (2024).
[29] Z. Zhang, A. Wang, X. Xu, and Y. Li, Measurement-efficient quantum Krylov subspace diagonalisation, Quantum **8**, 1438 (2024).
[30] M.-Q. He, D.-B. Zhang, and Z. D. Wang, Quantum Gaussian filter for exploring ground-state properties, Phys. Rev. A **106**, 032420 (2022).
[31] D. An, A. M. Childs, and L. Lin, Quantum algorithm for linear non-unitary dynamics with near-optimal dependence on all parameters, Commun. Math. Phys. **407**, 19 (2026), arXiv:2312.03916.
[32] K. Ghanem, A. Schuckert, and H. Dreyer, Robust extraction of thermal observables from state sampling and real-time dynamics on quantum computers, Quantum **7**, 1163 (2023), arXiv:2305.19322 [quant-ph].
[33] P. Guo, A. Shibu, J. Lin, and Y. Zhao, Imaginary time evolution of a quantum system through analytic continuation from real-time quantum simulation (2026), version 2, arXiv:2608.19943 [quant-ph].
[34] D.-B. Zhang, G.-Q. Zhang, Z.-Y. Xue, S.-L. Zhu, and Z. D. Wang, Continuous-variable assisted thermal quantum simulation, Phys. Rev. Lett. **127**, 020502 (2021).
[35] L. Bell, Y. Wang, K. C. Smith, Y. Liu, E. Dumitrescu, and S. M. Girvin, Co-designing spectral transformation oracles with hybrid oscillator-qubit quantum processors: From algorithms to compilation, PRX Quantum **6**, 040359 (2025).
[36] D. C. Sorensen, Numerical methods for large eigenvalue problems, Acta Numer. **11**, 519 (2002).
[37] K. Schreiber and H. Schwetlick, A Jacobi–Davidson like method for nonlinear eigenvalue problems based on singularity theory, PAMM **7**, 1020401 (2007).
[38] T. Kosugi, Y. Nishiya, H. Nishi, and Y.-i. Matsushita, Imaginary-time evolution using forward and backward real-time evolution with a single ancilla: First-quantized eigensolver algorithm for quantum chemistry, Phys. Rev. Research **4**, 033121 (2022).
[39] Sridhar, S. Bedkihal, and M. Bandyopadhyay, Coherent control of thermoelectric performance via engineered transmission functions in multidot Aharonov–Bohm heat engines, Phys. Rev. B **113**, 085428 (2026).
[40] S. Bedkihal, J. Behera, and M. Bandyopadhyay, Fundamental aspects of Aharonov–Bohm quantum machines: thermoelectric heat engines and diodes, J. Phys.: Condens. Matter **37**, 163001 (2025).
[41] H. Fawzi, O. Fawzi, and S. O. Scalet, Entropy constraints for ground energy optimization, J. Math. Phys. **65**, 032201 (2024).
[42] A. M. Childs, Y. Su, M. C. Tran, N. Wiebe, and S. Zhu, Theory of Trotter error with commutator scaling, Phys. Rev. X **11**, 011020 (2021).
[43] C. K. Law and J. H. Eberly, Arbitrary control of a quantum electromagnetic field, Phys. Rev. Lett. **76**, 1055 (1996).
[44] M. Hofheinz, H. Wang, M. Ansmann, R. C. Bialczak, E. Lucero, M. Neeley, A. D. O'Connell, D. Sank, J. Wenner, J. M. Martinis, and A. N. Cleland, Synthesizing arbitrary quantum states in a superconducting resonator, Nature **459**, 546 (2009).
[45] R. W. Heeres, B. Vlastakis, E. Holland, S. Krastanov, V. V. Albert, L. Frunzio, L. Jiang, and R. J. Schoelkopf, Cavity state manipulation using photon-number selective phase gates, Phys. Rev. Lett. **115**, 137002 (2015).
[46] W. Wang, L. Hu, Y. Xu, K. Liu, Y. Ma, S.-B. Zheng, R. Vijay, Y. P. Song, L.-M. Duan, and L. Sun, Converting quasiclassical states into arbitrary Fock state superpositions in a superconducting circuit, Phys. Rev. Lett. **118**, 223604 (2017).